

Journal of Materials Chemistry A

Accepted Manuscript



This is an *Accepted Manuscript*, which has been through the Royal Society of Chemistry peer review process and has been accepted for publication.

Accepted Manuscripts are published online shortly after acceptance, before technical editing, formatting and proof reading. Using this free service, authors can make their results available to the community, in citable form, before we publish the edited article. We will replace this *Accepted Manuscript* with the edited and formatted *Advance Article* as soon as it is available.

You can find more information about *Accepted Manuscripts* in the [Information for Authors](#).

Please note that technical editing may introduce minor changes to the text and/or graphics, which may alter content. The journal's standard [Terms & Conditions](#) and the [Ethical guidelines](#) still apply. In no event shall the Royal Society of Chemistry be held responsible for any errors or omissions in this *Accepted Manuscript* or any consequences arising from the use of any information it contains.

Controlled Mechanical Cleavage of Bulk Niobium Diselenide to Nanoscaled Sheet, Rod, and Particles Nanostructures for Pt-free Dye-sensitized Solar Cells

Mohammed Aziz Ibrahim,^{a,b,c} Wei-Chih Huang,^d Tian-wei Lan,^{a,b} Karunakara Moorthy Boopathi,^{b,e} Yu-Chen Hsiao,^d Chih-Han Chen,^d Widhya Budiawan,^{ab} Yang-Yuan Chen,^f Chia-Seng Chang,^f Lain-Jong Li,^g Chih-Hung Tsai,^{d,*} and Chih Wei Chu^{e,h,*}

^a Department of Physics, National Taiwan University, Taipei 106, Taiwan

^b Nanoscience and Technology Program, Taiwan International Graduate Program, Academia Sinica, Taipei 115, Taiwan

^c Department of Physics, Faculty of Science, University of Duhok, Duhok, Iraq

^d Department of Opto-Electronic Engineering, National Dong Hwa University, Hualien 97401, Taiwan E-mail: cht@mail.ndhu.edu.tw

^e Research Center of Applied Science, Academia Sinica, Taipei 115, Taiwan

^f Institute of Physics, Academia Sinica, Taipei 115, Taiwan

^g Institute of Atomic and Molecular Sciences Academia Sinica, Taipei 10617, Taiwan, ROC

^h Department of Photonics, National Chiao Tung University, Hsinchu 300, Taiwan E-mail: gchu@gate.sinica.edu.tw

Abstract

In this study, we report one-step process for the preparation of NbSe₂ nanosheets, nanorods and nanoparticles from pristine materials under the effects of shear and friction forces. Nevertheless, simple and facile methods for the large-scale syntheses of well-defined NbSe₂ nanostructures in high yield have yet to be realized and that will have a great impact in a wide range of applications. For example, developing Platinum (Pt)-free and highly efficient counter electrodes is meaningful and necessary for the cost reduction of dye-sensitized solar cells (DSSCs). By integrating this approach with a simple method of thin film preparation (spray coating) allowed us to prepare large-area, conductive, semitransparent flexible thin films of NbSe₂. We have used microscopic and macroscopic methods to examine the morphologies, compositions, crystallinity, and electrical and optical properties of the converted NbSe₂ nanostructures. DSSCs with NbSe₂ nanosheets counter electrode (CE) achieved a conversion efficiency of 7.73%, superior to an efficiency of 7.01% for Pt-based CE. Our NbSe₂ nanostructure provides a cost-effective CE alternative to the noble metal Pt in DSSCs.

Introduction

Two-dimensional (2D) nanostructures have received much attention since the discovery of graphene in 2004.¹ In addition, transition metal dichalcogenides (TMDs), a group of 40 different types of inorganic layered compounds combining transition metals (M; e.g., W, Mo, Ti, Nb, Ta) and chalcogens (X; S, Se, Te)²⁻⁴ in an MX_2 stoichiometry, are extremely promising building blocks for the development of many next-generation applications, including superlubricants,⁵ superconductors,⁶ batteries,⁷ solar cells,⁸ DSSCs,⁹ thin-film transistors,^{10, 11} LEDs,¹² UV range photodetectors,¹³ and transparent conducting electrodes.¹⁴ Crystallographically similar to graphite, the sandwich layers are stacked together by van der Waals interactions; therefore, MX_2 species have the propensity to delaminate into individual nanosheets comprising only a few atomic layers. Depending on the combination of metal and chalcogen, TMDs can be metallic, semimetallic, or semiconducting; for example, tungsten sulfide (WS_2) and molybdenum sulfide (MoS_2) are usually semiconducting, while niobium selenide (NbSe_2) is metallic.¹⁵ Among the TMDs, it has been demonstrated recently that NbSe_2 precursor is a particularly excellent model system for processing and fabricating rich inorganic nanostructures using various methods.¹⁶ The metallic behavior of NbSe_2 arises from the fact that within the sandwich layer each Nb atom is coordinated to six selenide atoms in the form of a trigonal prism (see Fig. S1, Supporting Information), similar to the corresponding structures of WS_2 and MoS_2 , except that Nb has one less d electron than Mo or W in its valence shell; the Fermi energy is, therefore, shifted to the d band.¹⁷

Several synthesis techniques have been proposed in the past decade for the production of TMD nanostructures, including liquid exfoliation,^{18, 19} intercalation-assisted exfoliation,^{20, 21} chemical vapor deposition,²² hydrothermal methods,^{23, 24} solvothermal methods,²⁵ microwave

methods,²⁶ and mechanochemistry (high energy ball-milling).⁸ Generally, layered crystals can be synthesized to form highly anisotropic compounds that readily cleave along a preferred plane. Mechanically peeled 2D sheets typically feature fewer defects than those produced using chemical methods.²⁷ If a mechanical process can be developed to treat tens of thousands of particles in a single run and to peel each particle hundreds of times, a large number of high-quality nanosheets could be harvested for studies of their properties and for their practical applications. For these reasons, there is a strong motivation for systematic and fundamental investigations of growth control mechanisms related to NbSe₂ parent compounds.

A typical DSSC consists of a transparent conductive substrate, a porous thin-film photoelectrode composed of TiO₂ nanoparticles, dyes, an electrolyte, and a CE.^{28, 29} The CE, as one important component in DSSCs, is usually composed of a conductive catalytic layer. The requirements for the CE in DSSCs are low charge-transfer resistance and high exchange current densities for effective reduction of the oxidized species, and good chemical/electrochemical stability in the electrolyte systems.^{30, 31} Due to the high electrocatalytic activity and good chemical stability, in most cases Pt is used as the CE material to obtain high efficiency DSSCs. However, as a noble metal, Pt is relatively expensive, which is big obstacles for the large-scale application of DSSCs.^{9, 30} Therefore, to developing Pt-free and highly an efficient CE is meaningful and necessary for the cost reduction of dye-sensitized solar cells. Here, we developed a simple but effective approach for exfoliating ultrathin nanosheets from bulk powder and then fracturing them into nanorods and finally breaking them into nanoparticles (nano-platelet) in high yield through control over the imposing time in one-step process. Because of its metallic prosperity and high electrocatalytic activity and reversibility in the I₃⁻/I⁻ redox reaction, we used NbSe₂ nanostructures as Pt replacement CE in DSSCs. Unlike previously reported approaches of

TMD preparations, our solution-based method is rapid, easy, cheap, and insensitive to ambient conditions; it does not require a third-phase dispersant (i.e., surfactant), it consumes low amounts of energy, and it can potentially be scaled up to give large quantities (liters) of dispersions of exfoliated materials (see Fig. S2, Supporting Information) exhibiting high stability over long periods of time (at least six months; see sedimentation tests in Fig. S3, Supporting Information). According to our knowledge, this is the first time that three different types (shape and size) of nanomaterials can be produced in one step process. Considering the generality of this simple realization of exfoliated NbSe₂ nanomaterials, our method might stimulate interest in the growth of a very broad range of TMD systems exhibiting various properties and functionalities. By integrating this approach with a simple method of thin film preparation allowed us to prepare large-area thin films. When these nanomaterials used as CE in DSSCs, results showed that DSSCs based on NbSe₂ nanosheets CE achieved a higher efficiency than Pt-based CE.

Experimental Section

Nanomaterials preparation. The homemade wet grinding machine used to prepare the NbSe₂ nanomaterials is presented in Scheme S1. First, NbSe₂ powder (99.9%; Alfa Aesar) was mixed with pure *N*-methyl-2-pyrrolidinone (NMP, 99 % Macron Chemical, USA) at a concentration of 0.5 wt%. Approximately 50% of the container was filled with micro-sized zirconia beads (size, 100 μm; density, ~ 5.95 g/cm³); the remaining volume was a suspension of the particles to be ground. The peripheral speed of the rotor was fixed at 2000 rpm. A water-cooled circulation allowed the temperature to be controlled during the size-reduction process. The bright red dispersion was purified without any contamination from the zirconia beds, which were highly dense and, therefore, precipitated readily after grinding to the bottom of the container.

Microscopic and Spectroscopic observation. The ground dispersion of the nanomaterial was diluted tenfold with isopropyl alcohol (IPA, 99 %; Alfa Aesar); drops of the solution were placed on a holey carbon-coated copper grid (Lacey Carbon Type-A 300 mesh copper grid; TED Pella) or Si/SiO₂ and then dried in air at 70 °C prior to characterization using TEM (JEM 2100F), SEM (FEI Nova200), AFM (Veeco di Innova) coupled with XPS (PHI 5000 Versa Probe scanning ESCA microprobe), and Raman spectroscopy (NT-MDT confocal Raman microscopic system; exciting laser wavelength: 514 nm; laser spot size: 0.5 μm). TMD powders before and after grinding were characterized using XRD (PANalytical).

NbSe₂ thin film and CEs fabrication. NbSe₂ nanomaterial thin films were fabricated by using simple spray deposition method. The spray-coating set-up was developed in conventional environment (air) under chemical hood. We used a simple dual action commercial airbrush (MECAFER AG-1) supplied by a nitrogen line and fixed on a mechanic arm over a hot plate (for the control of substrate temperature during the spray). The PET substrates cleaned in ultrasonic bath with acetone and IPA (10 min each step). The dispersion of the nanomaterials was first diluted with IPA with 1:1 ratio in order to speed up the drying process. The solution was pumped into the air stream in the spray nozzle continuously on PET substrate. By controlling the nozzle diameter and adjusting the distance between the sample and sprayer head, very uniform thin films were fabricated. After the spray deposition, thin films were left in air for 1 h to dry. NbSe₂ CEs were fabricated by depositing NbSe₂ nanostructure materials on the fluorine doped tin oxide (FTO) glass plates using drop casting method. The FTO glasses coated with NbSe₂ were then annealed under a N₂ atmosphere at 500 °C for 30 min in a tube furnace to form the NbSe₂ CEs. Pt CE of the DSSC was prepared by coating the paste of chemical Pt precursor (Platinum (II) acetylacetonate, 99.99% trace metals basis, Sigma-Aldrich) on the FTO glass

plates by doctor-blade method. After heating at 450°C for 20 minutes, a quasi-transparent activated Pt layer was obtained.

Magnetic Susceptibility measurement. The zero field cool (ZFC) susceptibility measurement was performed by using a superconducting quantum interference device magnetometer (SQUID, Quantum Design Inc.). The samples were cooled in zero fields from 0 K temperatures in a strong magnetic field (FC). Then samples were heated gradually while measuring magnetization (M) with constant field.

Electrical and Optical measurements. The optical properties (absorption and transmittance spectra) of thin films were recorded using a Jasco V-670 UV–Vis–NIR spectrophotometer. While the conductivities were measured at room temperature using the van der Pauw four-point probe technique with a Hall effect measurement system (Ecopia, HMS 5000).

Characterization of the CEs. The cyclic voltammetry (CV) was employed to characterize the relative catalytic ability of the CEs. The CV measurements were conducted using a three-electrode electrochemistry system. Pt or NbSe₂ CEs under testing were used as the working electrode, Pt foil as the counter electrode, and Ag/Ag⁺ as the reference electrode. The scan rate used was 50 mV/s, while the electrolyte was the acetonitrile solution containing 10 mM LiI, 1 mM I₂, and 100 mM LiClO₄.

Fabrication of DSSCs. To prepare the DSSC working electrodes, the FTO glass plates were first cleaned in a detergent solution using an ultrasonic bath for 15 min, and then rinsed with water and ethanol. A layer of 20-nm-sized anatase TiO₂ nanoparticles (nanopowder, 99.99% trace metals basis (Aldrich)) for the transparent nanocrystalline layer was first coated on the FTO glass plates by the doctor-blade method. After drying the film at 120 °C, another layer of anatase TiO₂ nanoparticles was then deposited as the light

scattering layer of the DSSC. The resulting working electrode was composed of a 12- μm -thick transparent TiO_2 nanoparticle layer (particle size: 20 nm) and a 4- μm -thick TiO_2 scattering layer (particle size: 400 nm). The nonporous TiO_2 electrodes were then sequentially heated at 150 °C for 10 min, at 300 °C for 10 min, at 400 °C for 10 min, and finally, at 500 °C for 30min. After cooling, the nonporous TiO_2 electrodes were immersed into a dye solution at room temperature for 24 hours for dye adsorption. The dye solution was composed of 0.5 mM well-known ruthenium dye **N719**, [cis-di(thiocyanato)-N-N'-bis (2,2'-bipyridyl-4-carboxylic acid-4'-tetrabutyl-ammonium carboxylate) ruthenium (II)], and 0.5 mM chenodeoxycholic acid (CDCA, as a co-adsorbent) in the acetonitrile/*tert*-butanol mixture (1:1). Various CEs for the DSSCs were prepared as described in the previous section. The dye-adsorbed TiO_2 working electrode and a CE were then assembled into a sealed DSSC cell with a sealant spacer between the two electrode plates. A drop of electrolyte solution [0.6 M 1-butyl-3-methylimidazolium iodide (BMII), 0.03 M I_2 , 0.5 M 4-*tert*-butylpyridine, and 0.1 M guanidinium thiocyanate in a mixture of acetonitrile–valeronitrile (85: 15, v/v)] was injected into the cell through a drilled hole. Finally, the hole was sealed using the sealant and a cover glass. An anti-reflection coating film was adhered to the DSSC. A mask with an aperture area of 0.125 cm^2 was covered on a testing cell during photocurrent-voltage and incident photon-to-current conversion efficiency measurements.

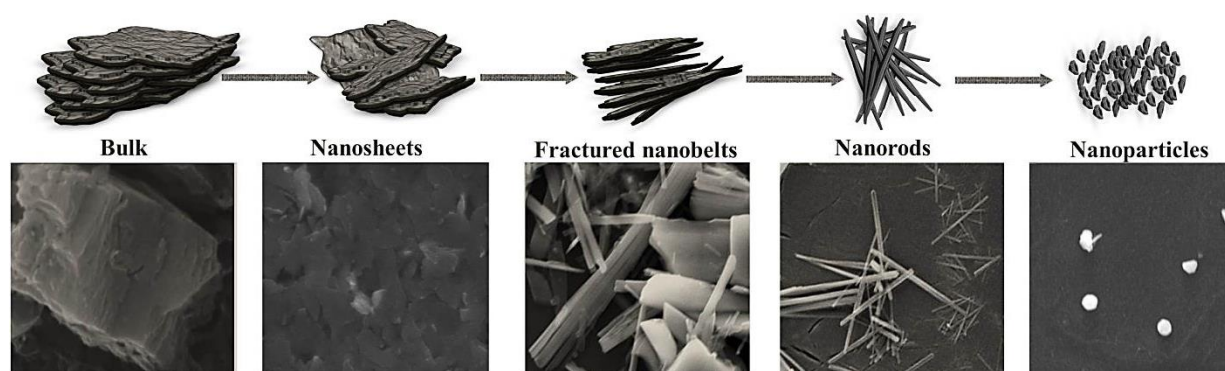
DSSCs characterizations. The photocurrent-voltage (I-V) characteristics of the DSSCs were measured under illumination of the simulated AM1.5G solar light from a 550-W Xenon lamp solar simulator. The incident light intensity was calibrated to be 100 mW/cm^2 by using a reference Si photodiode equipped with an IR-cutoff filter (KG-5, Schott) to reduce the spectrum mismatch in the region of 350-750 nm between the simulated light and AM 1.5G to less than 2%.

The reference cell is certificated by Bunkoh-keiki Co Ltd, Japan. I-V curves were obtained by applying an external bias voltage to the cell and measuring the generated photocurrent. The incident monochromatic photon-to-current conversion efficiency (IPCE) spectra were measured by using a 150-W Xenon arc lamp as the light source coupled to a monochromator. The IPCE data were taken by illuminating monochromatic light on the solar cells (with a wavelength sampling interval of 5 nm from 300 nm to 750 nm) and measuring the short-circuit current of the solar cells. The IPCE measurement was performed under the full computer control. The electrochemical impedance spectroscopy (EIS) of the cells was measured by using an impedance analyzer with a frequency range of 0.1 Hz~1 MHz. In this study, during the impedance measurement, the cell was under the constant illumination (AM 1.5G 100 mW/cm²). The impedance of the cell (throughout the frequency range of 0.1 Hz to 1 MHz) was then measured by applying a bias at the open-circuit voltage (V_{OC}) of the cell (namely, under the condition of no DC electric current) and by using an AC amplitude of 10 mV.

Results and Discussion

Scheme 1 presents a growth mechanism for the NbSe₂ nanostructures. Bulk NbSe₂ possesses a hexagonal close packed structure, with the (001) surface being the most densely packed and representing the largest d-spacing plane; thus, the pathway of plastic deformation (fracture) of highly anisotropic NbSe₂ prefers to proceed via delamination of specific (001) layers.^{32, 33} Indeed, when beads collide, the fluid squeezed between the two surfaces of contact slows down their approaching motion, due to lubrication, and the materials will be subjected to two distinct mechanical phenomena: either squeezed between two colliding beads or between a bead and a wall, thereby experiencing high pressure and high temperature generated locally in the powder (so-called hot spots) during the milling process.^{34, 35} During mechanical cleavage, the materials

are subjected to severe plastic deformation that exceeds their mechanical strength. In fact, shear and plastic deformations play important roles in the formation of defects and in the occurrence of phase transformations during grinding.³⁶ The pulling force can easily break the weak van der Waals interactions between layers, resulting in a single or a few layers of smaller size being peeled away from the surface that will be break-down by fractional forces. Further imposing the materials to shear and friction forces can directly affect both their shape and size (see Fig. S4, Supporting Information). The resultant layers are repeatedly flattened fractured and welded the two basic events through which an ultrathin layer is ruptured along the pathway of the plastic deformation; that is, energy-minimization favors one-dimensional shapes, as observed using microscopes, which can clearly reveal the cleavage process (Fig. 1). In addition, figure S5 (supporting information) show a TEM with typical high-resolution (HRTEM) image of the fractured nanosheets. The direction of fractured sheet, show a structure with the [001] crystallographic orientation, in conjunction with the selected-area electron diffraction (SAED) pattern (inset in Fig. S5) recorded along (001) zone axis. The (110) direction of the SAED pattern is parallel to the rod axis, and thus shows that fracturing occurs along the (001) direction.



Scheme 1. Schematic representation and corresponding SEM images of the conversion process: A three-dimensional network of bulk NbSe₂ is converted to 2D nanosheets (6hr), 1D nanorods (10hr), and then to 0D nanoparticles (12hr) under the impact and friction of beads.

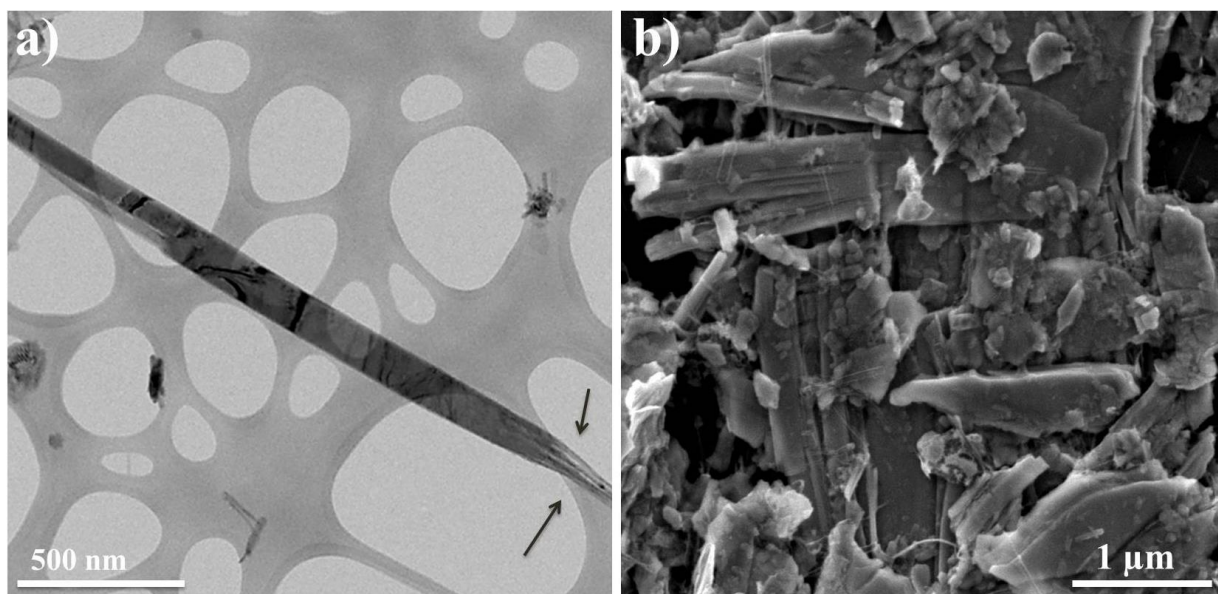


Figure 1. Microscopy images after one of the conversion stages: (a) TEM, and (b) SEM images of ruptured nanosheets of NbSe₂. The starting fractured area in (a) shown by arrows.

We used SEM and AFM to characterize the morphologies of the as-synthesized NbSe₂ nanomaterials. SEM analysis of the pristine NbSe₂ (see Fig. S6, Supporting Information) revealed a very thick (>100 μm), disordered, network arrangement of 2D sheets; in comparison, the ground materials were very thin, separate nanosheets, nanorods, and nanoparticles. Nanosheets are with typical lateral dimensions between 100-500 nm (Fig. 2a). The nanorods had lengths up to 1.2 μm and diameters ranging from 20 to 100 nm (Fig. 2b), while nanoparticles had an average size of 50-100 nm (Fig. 2c). The AFM images (figs. 2d, 2e, and 2f) also revealed the same dimensions of the nanostructures with majority having an average thickness of approximately < 8 nm for nanosheets, < 5 nm for nanorods, and < 3 nm for nanoparticles (Fig. S7, supporting information).

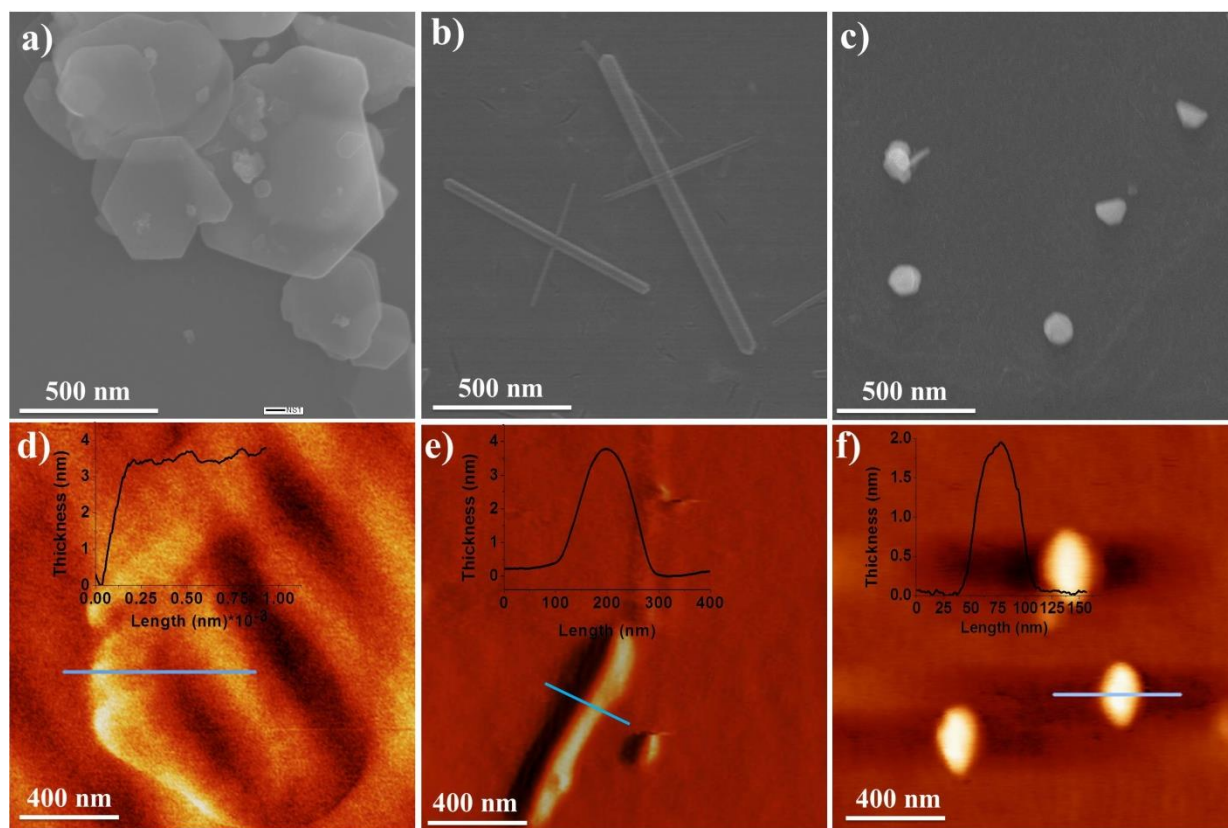


Figure 2. Morphology of the NbSe₂ nanostructures: (a, b, and c) SEM image of different sizes nanosheets, nanorods, and nanoparticles, respectively. (d, e, and f) AFM height images of a typical nanosheets, nanorods, and nanoparticles, respectively. The insets of AFM images are corresponding height profiles.

We used TEM imaging and diffraction analysis to determine the crystal structures of individual nanostructures. Figures 3a, 3d, and 3g present TEM images of a typical nanosheet, nanorod and nanoparticles, respectively; Figs. 3b, 3e, and 3h provide SAED patterns of flat areas of the nanosheet, nanorod and nanoparticles. HRTEM of a nanosheet on its edge revealed a spacing of 6.3 Å, which corresponds to the separation between (002) planes and hexane width of 3.03 Å (Fig. 3c). Hence, the structures of three nanostructures were equivalent and were similar to that of the bulk NbSe₂. HRTEM indicated that the individual nanorod and nanoparticle were crystalline (Fig. 3f and 3i), with the longitudinal axis of the nanorods perpendicular to the [002] direction.³⁷ The SAED patterns of a number of different nanorods and nanoparticles revealed the

same crystallinity as the nanosheets. In addition, these SAED patterns were consistent with the XRD patterns (Fig. 4a), which were similar to those of the 2D nanosheets, confirming that no distortion occurred upon flattening and fracturing these materials. The few-layer nanosheets were typically a few hundred nanometers in length, in agreement with previous reports;^{15, 18} an ultrathin nanorod having a length of a few hundred nanometers and a width of approximately 25 nm in width with a thick coating-like amorphous structure on the rods surface at about 2 nm (Fig. 3f), the nanoparticles were having an average size of 50 nm are presented here (Fig. 3d and 3g) and in the SEM image in figure 2b and 2c. The (001) direction of the SAED pattern is parallel to the rod axis, and thus shows that fracturing occurs along the (001) direction.

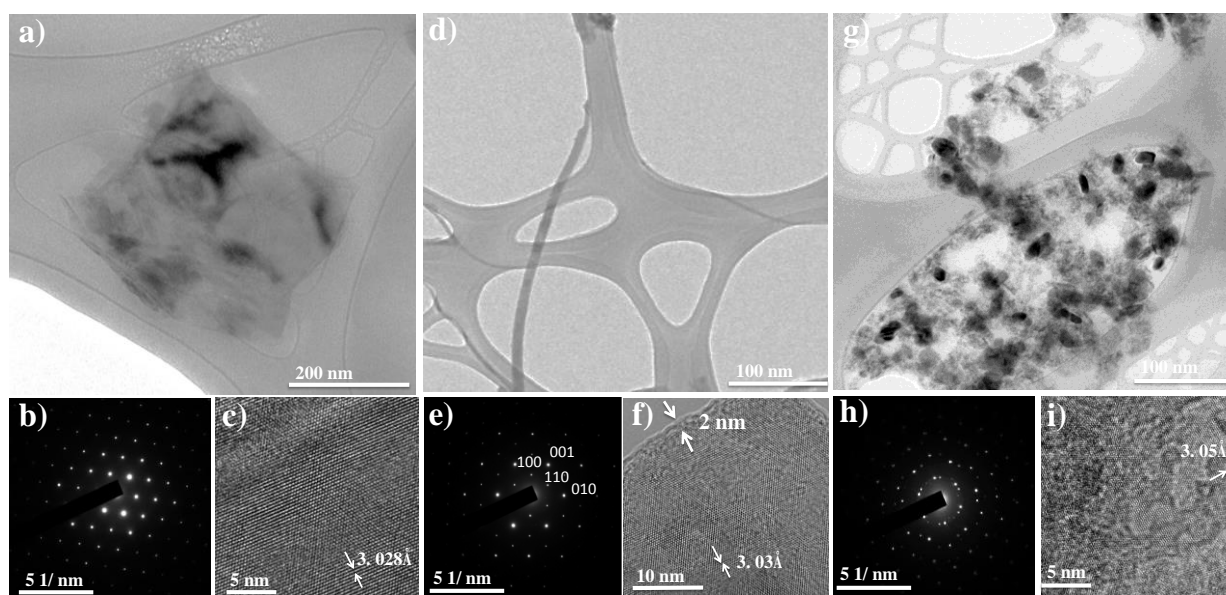


Figure 3. TEM analysis of NbSe₂ nanostructures: (a, d, and g) TEM images, (b, e, and h) SAED patterns, and (c, f, and i) HRTEM images of (a–c) a typical ultrathin NbSe₂ nanosheet, (d–f) a typical ultrathin NbSe₂ nanorod, and (g–i) a typical NbSe₂ nanoparticles.

Next, we used XRD to study the phase change of the sample (Fig. 4a). The nearly identical diffraction angles (2θ) of the peaks before and after grinding imply the same degrees of crystallinity, with the decreased intensity and broadening of the peaks after grinding, from bulk to sheets, rods and then to particles, being consistent with decreased lateral sizes. The

corresponding diffraction peaks for the samples before and after grinding can be indexed to highly crystalline hexagonal NbSe₂ (JCPDS File No. 018–0923), at which the four diffraction peaks that located approximately at 2θ values of 14.00, 30.38, 36.92 and 46.06 can be assigned to the reflections of the (002), (101), (103) and (110) planes, respectively; they suggested that the as-prepared NbSe₂ nanomaterials were oriented predominantly along the c -axis, or the [002] direction,^{3,38} consistent with the HRTEM data in Fig. 3. We further confirmed the production of the NbSe₂ nanomaterials using Raman spectroscopy. The Raman spectrum ($\lambda_{\text{excitation}} = 514 \text{ nm}$) in figure 4b features three main bands at 220, 267, and 284 cm^{-1} that match well with the values reported previously for NbSe₂ single crystals.^{39, 40} Again, this finding suggests that the crystal structure of NbSe₂ was preserved satisfactorily during the milling treatment.

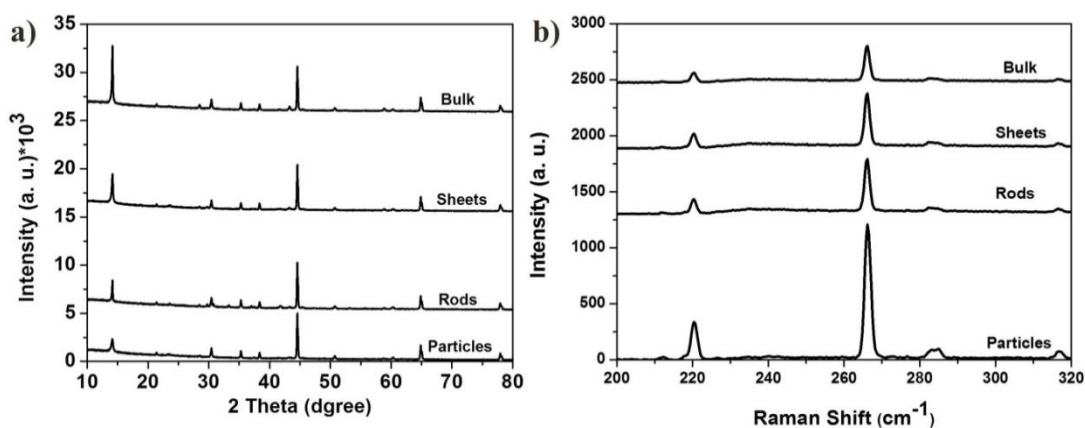


Figure 4. Structural analysis of NbSe₂ nanostructures: (a) Powder XRD patterns of bulk NbSe₂ and resulting nanostructures (hexagonal; JCPDS: 01-089-4313; $a = b = 3.0 \text{ \AA}$; $c = 12.547 \text{ \AA}$). Periodicity in the c -axis is evident for the bulk material, with a strong (002) peak observed at a value of 2θ of 14° . (b) Raman spectra ($\lambda_{\text{excitation}} = 514 \text{ nm}$) of the bulk NbSe₂ and NbSe₂ nanostructures.

In addition, we used XPS, energy dispersion spectroscopy (EDS) spectrum, and X-ray fluorescence (XRF) to investigate the stoichiometry of the nanomaterials. We assign the peaks at 202.3 and 205.2 eV in the XPS spectrum of the niobium diselenide (Fig. S8, Supporting Information) to the Nb 3d_{5/2} and Nb 3d_{3/2} orbitals, respectively, with those at 58 and 55.3 eV

representing the Se 3d_{5/2} and Se 3d_{3/2} orbitals, respectively. These binding energies for the Nb 3d and Se 3d peaks are consistent with oxidation states of Nb⁴⁺ and Se²⁻ in NbSe₂.^{37, 41} From the EDS spectrum in figure S9 (Supporting Information), we estimated the atomic ratio of Nb to Se in nanorods and nanoparticles to be close to 1:2, giving the samples an empirical formula of NbSe₂, as confirmed through XRF-based elemental analysis, which provided a Nb-to-Se ratio of approximately 1:2.

To examine whether the grinding process changed the physical properties of the pristine NbSe₂ structure, we examined the superconductivity of the nanostructures. Figure 5a reveals the temperature-dependent magnetization of these samples in zero field cooled AC susceptibility measurements. The existence of superconductivity of the resultant NbSe₂ is confirmed by the strong Meissner effects⁴² of the nanosheets, rods, and particles at transition temperatures (T_c) of 6.96, 7.084, and 6.89 K, respectively; these values are slightly greater than that of bulk NbSe₂ (T_c = ca. 7.2). We observed these transitions consistently in all of our samples; unlike the sharp transition of the bulk sample, however, the nanostructures exhibited broadening and depression of their T_c signal amplitudes, possibly as a result of the nanosized effect and contamination by impurities (e.g., O atoms), respectively. This finding also implied that the superconducting phase fraction was small in the nanosized samples.⁴³

We used spray coating to prepare very uniform, continuous semitransparent, flexible thin film from the resultant nanostructure materials (Fig. 5d and Fig. S10, Supporting Information). We investigated the flexibility of the thin film by using the conductivity as a parameter and exploring its stability under various bending conditions. Figure 5b displays the correlation between the bending angle and the conductance of the nanomaterials-containing film. This film exhibited comparable conductance before and after performing the bending test cycle,

for example nanorods film has a conductivity of 5.88 and 5.85 S/cm, respectively by virtue of its high flexibility and mechanical strength. Figure 5c presents transmittance spectra of the films on PET substrates. We controlled the thickness of the films to minimize absorption in the visible region while maintaining sufficient conductivity to allow good carrier transport; the film thickness was approximately 230–250 nm (estimated using AFM) and the transmittance at 550 nm was greater than 55%. In addition, we calculated the figures of merit for our transparent conducting films to compare them in the context of other transparent flexible thin films. The figure of merit of NbSe₂ film on PET was approximately 1; this value is superior to those of all published data for corresponding graphene-containing films^{13, S1} (see Section S4 and Fig. S10 and S11, Supporting Information).

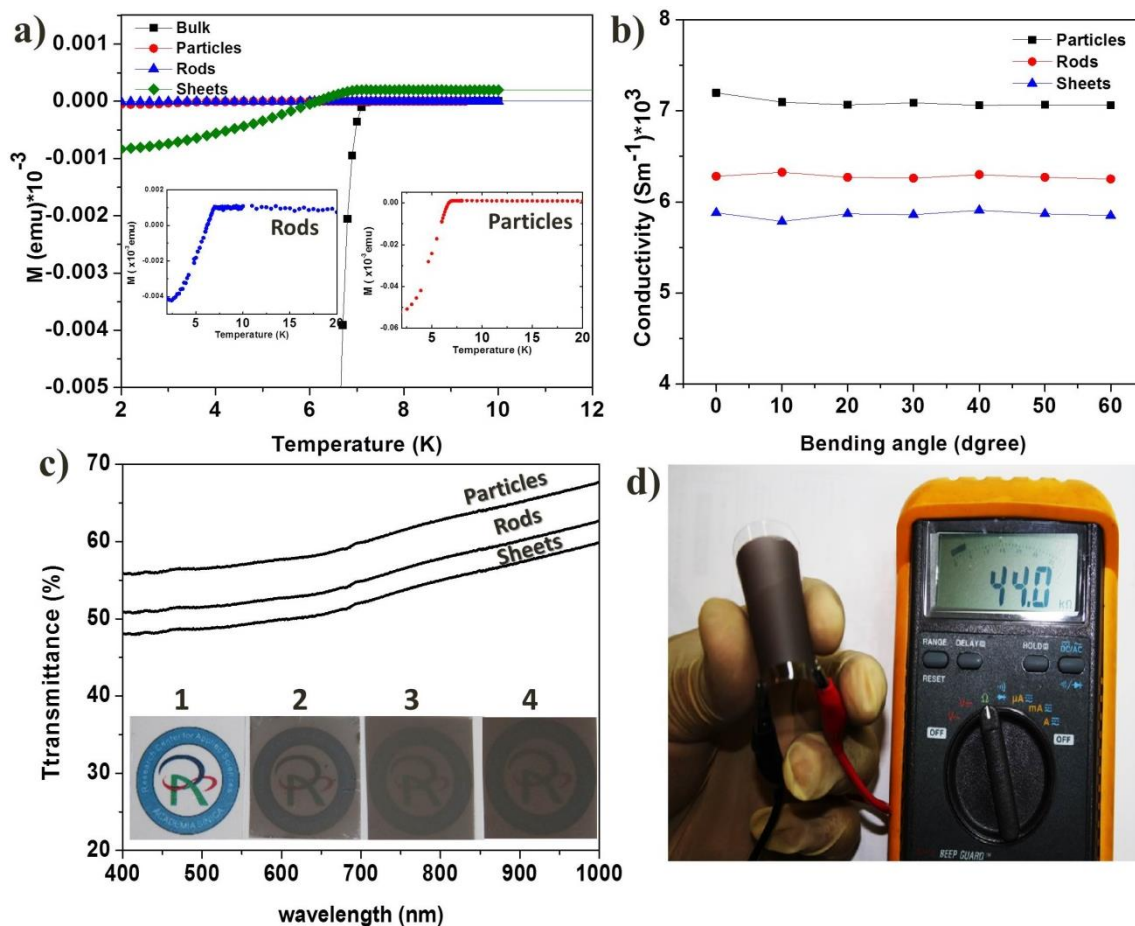


Figure 5. Superconductivity measurements, bending tests, and transmittance of thin films: (a) Magnetic susceptibility plotted with respect to temperature for the pristine NbSe₂, the NbSe₂ nanosheets, and a powder containing a bundle of NbSe₂ nanorods and nanoparticles. Inset: Magnified view of the superconductivity transition for the NbSe₂ nanorods (left) and nanoparticles (right). (b) Conductivity of a thin film of NbSe₂ on a PET substrate, plotted with respect to the bending angle. (c) Transmission spectra of films of the NbSe₂ nanostructures. Inset: Photograph of the (1) bare PET substrate, (2) film of nanoparticles on PET, (3) film of nanorods on PET, and (4) film of nanosheets on PET. (d) Representative photograph of a film as a flexible electrode subjected to bending.

As a proof of principle and to highlight the importance of our findings, we used these NbSe₂ nanostructure materials as Pt replacement CE in DSSC. Figure 6a shows the cyclic voltammograms of the I₃⁻/I⁻ redox couple for Pt and NbSe₂ CEs. In general, the magnitude of the cathodic current peak represents the catalytic capability of a CE toward reduction of I₃⁻ in DSSCs. Among the four CEs, the NbSe₂ nanosheets exhibited the highest cathodic current. Compared to the Pt CE, the NbSe₂ nanosheets CE possesses a larger reduction peak current, indicating better electrocatalytic activity and reversibility in the I₃⁻/I⁻ redox reaction. In contrast, the NbSe₂ nanoparticles and nanorods CEs show reduced peak current densities, indicating their lower electrocatalytic activity in the I₃⁻/I⁻ redox reaction. The CV results suggest that depositing NbSe₂ nanosheets on FTO glass plates be an effective way to increase the active surface areas of the CEs and thus to enhance their electrocatalytic ability. The enhanced electrocatalytic activities of NbSe₂ nanosheets CE is due to the largest surface areas and better coverage on the FTO glass substrates. The coverage rate of these nanostructures can be indicating from the morphology given in SEM images (Fig. S12, Supporting Information). The NbSe₂ nanoparticles CE shows a flat film surface, the NbSe₂ nanosheets sample exhibits an intercrossed nanosheet conglomeration, and the NbSe₂ nanorods sample presents irregular nanorod structures. Among the three NbSe₂ CEs, the NbSe₂ nanosheets CE exhibits the largest surface areas and best coverage on the FTO glass substrates.

The photovoltaic characteristics of Pt, NbSe₂ nanoparticles, nanosheets, and nanorods as the CEs in DSSCs were evaluated with a sandwich DSSC cell. Figure 6b and 6c show the I-V and IPCE characteristics, respectively, of the DSSCs using various CEs and device parameters are summarized in Table I.

Table I. Characteristics of DSSCs fabricated using various CEs. PCEs were averaged over 10 solar cells.

Counter electrode	Jsc (mA/cm ²)	Voc (V)	Fill Factor	Efficiency (%)
Pt	15.59	0.72	0.62	7.01
NbSe ₂ nanoparticles	14.93	0.75	0.55	6.27
NbSe ₂ nanosheets	16.85	0.74	0.62	7.73
NbSe ₂ nanorods	14.85	0.74	0.46	5.05

The DSSC based on Pt CE shows an overall conversion efficiency of 7.01%. Under the same conditions, DSSCs based on NbSe₂ nanosheets CE exhibit a higher power conversion efficiency of 7.73%. On the other hand, DSSCs based on NbSe₂ nanoparticles and nanorods CEs show inferior conversion efficiencies of 6.27% and 5.05%, respectively. This lower efficiency mainly comes from a relatively low fill factor (FF) which is owing to the small surface areas and low coverage on FTO substrates. Such results indicate that the NbSe₂ nanosheets could provide cost-effective CEs alternative to the noble metal Pt in DSSCs due to its high surface areas and coverage.

Further investigation on the higher device parameters of NbSe₂ nanosheets CE is given by using the IPCE spectra of the DSSCs based on various CEs as shown in Fig. 6c. Among these four CEs, DSSC based on NbSe₂ nanosheets exhibits the best spectral response. The peak increases from ~84% of the DSSCs based on Pt, to ~89% of the DSSCs based on NbSe₂

nanosheets. In contrast, DSSCs based on NbSe₂ nanoparticles and nanorods CEs show relatively lower IPCE peaks value, indicating their inferior short-circuit current values. The IPCE results are in accordance with the short-circuit currents of the DSSCs.

The DSSCs were further characterized by electrochemical impedance spectroscopy (EIS). EIS is a useful tool for characterizing important interfacial charge-transfer processes in DSSCs, such as the electron transfer/charge recombination at the TiO₂/dye/electrolyte interface, electron transport in the TiO₂ electrode, electron transfer at the CE, and I₃⁻ transport in the electrolyte etc.^{44, 45} Figure 6d shows the EIS Nyquist plots (*i.e.*, minus imaginary part of the impedance, $-Z''$, vs. the real part of the impedance, Z' , when sweeping the frequency) for DSSCs based on various CEs. For the frequency range investigated (0.1 Hz to 1 MHz), three regimes are generally distinguished: a small semicircle in the lowest frequency range (~ 0.1 Hz to 1 Hz), a larger semicircle in the middle frequency range (~ 1 Hz to 1 kHz), and another smaller semicircle in the highest frequency range (>1 kHz). With the bias illumination and voltage applied, the small semicircle at lowest frequencies is associated with ion diffusion in the electrolyte; the larger semicircle at middle frequencies corresponds to the charge-transfer processes at the TiO₂/dye/electrolyte interface, while the smaller semicircle at highest frequencies corresponds to the charge-transfer processes at the CE/electrolyte interface.³⁰ Among these four CEs, the smallest width of middle-frequency semicircle in the EIS was observed in the DSSCs based on NbSe₂ nanosheets CE, which indicates the most efficient electrocatalytic activity for I₃⁻ reduction and electron generation and thus larger electron population at its TiO₂/dye/electrolyte interface. The EIS results are in good agreement with results of the short-circuit currents and the overall power conversion efficiencies of the DSSCs.

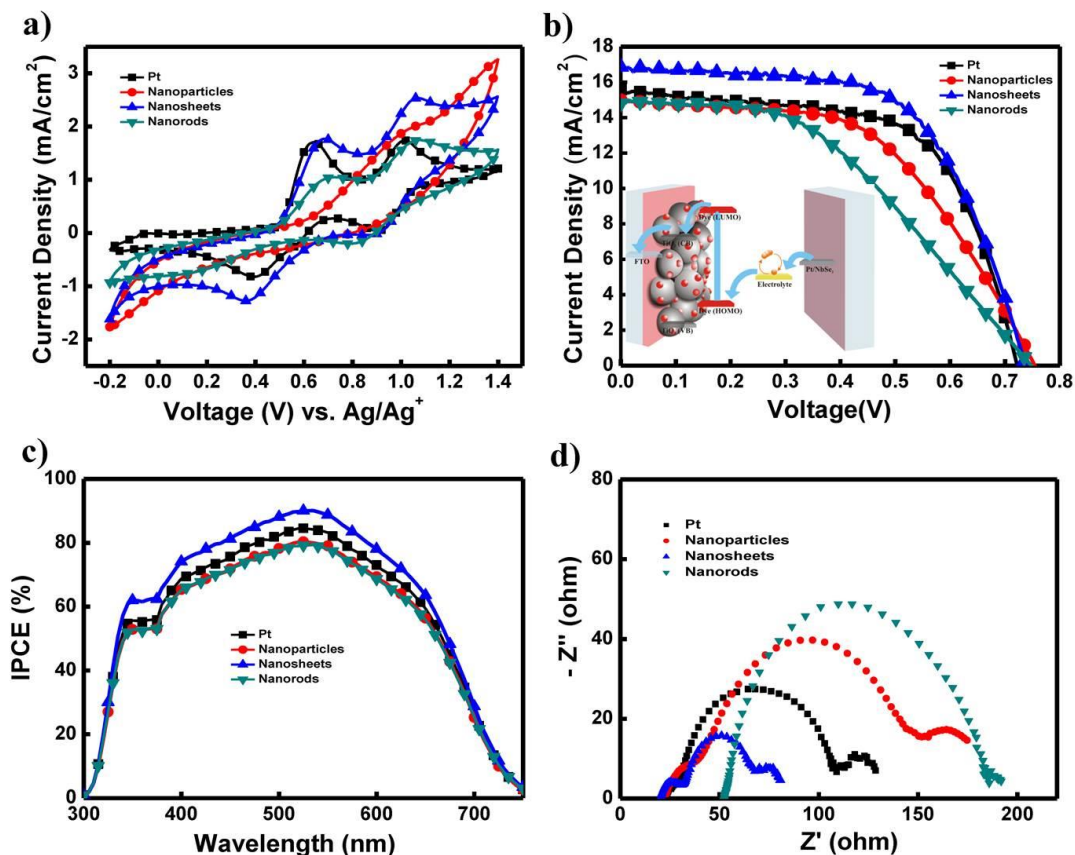


Figure 6. (a) Cyclic voltammograms of Pt and various NbSe₂ CEs. (b) J-V curves, (c) IPCE curves, and (d) EIS Nyquist plots of DSSCs based on Pt and various NbSe₂ CEs. The inset of (b) is the schematic representation of DSSC device structure with energy level diagram of the component materials used for device fabrication.

Conclusion

In conclusion, we have developed a novel and feasible approach with control over the milling time for converting layered bulk NbSe₂ to low dimensional materials under the influence of mechanical forces. This very simple technique has the potential for scaling up to mass production at low cost, offering a promising opportunity to produce nanomaterials in the volumes required for real-world applications. When these nanostructures materials used as CEs in DSSC, NbSe₂ nanosheets CE showed the highest power conversion efficiency compared to nanorods, nanoparticles, and Pt CEs. Such results indicate that the NbSe₂ nanosheets could provide cost-effective CEs alternative to the noble metal Pt in DSSCs due to its high surface

areas and coverage. In addition, this approach should lead to the preparation of thin films of inorganic layered compounds for applications in batteries and other devices, as well as the production of a wide range of hybrids with tunable conductivity, attractive thermoelectric properties, and enhanced mechanical properties.

Acknowledgments

We thank the National Science Council (NSC), Taiwan (NSC 102-2221-E-001-029-MY2 and NSC 102-2221-E-259-025), for financial support. Dr. Chu is grateful for technical support from Nano Core, the Core Facilities for Nanoscience and Nanotechnology at Academia Sinica in Taiwan.

References

1. A. K. Geim and K. S. Novoselov, *Nat Mater*, 2007, **6**, 183-191.
2. M. Xu, T. Liang, M. Shi and H. Chen, *Chemical reviews*, 2013, **113**, 3766-3798.
3. X. Huang, Z. Zeng and H. Zhang, *Chemical Society reviews*, 2013, **42**, 1934-1946.
4. M. Chhowalla, H. S. Shin, G. Eda, L.-J. Li, K. P. Loh and H. Zhang, *Nat Chem*, 2013, **5**, 263-275.
5. L. Rapoport, A. Moshkovich, V. Perfilyev, A. Laikhtman, I. Lapsker, L. Yadgarov, R. Rosentsveig and R. Tenne, *Tribology Letters*, 2011, **45**, 257-264.
6. V. V. Ivanovskaya, A. N. Enyashin, N. I. Medvedeva and A. L. Ivanovskii, *physica status solidi (b)*, 2003, **238**, R1-R4.
7. H. Liu, D. Su, R. Zhou, B. Sun, G. Wang and S. Z. Qiao, *Advanced Energy Materials*, 2012, **2**, 970-975.
8. M. A. Ibrahim, T.-w. Lan, J. K. Huang, Y.-Y. Chen, K.-H. Wei, L.-J. Li and C. W. Chu, *RSC Advances*, 2013.
9. J. Guo, Y. Shi, C. Zhu, L. Wang, N. Wang and T. Ma, *Journal of Materials Chemistry A*, 2013, **1**, 11874-11879.
10. C. Ataca, H. Şahin and S. Ciraci, *The Journal of Physical Chemistry C*, 2012, **116**, 8983-8999.
11. RadisavljevicB, RadenovicA, BrivioJ, GiacomettiV and KisA, *Nat Nano*, 2011, **6**, 147-150.
12. K. J. Reynolds, G. L. Frey and R. H. Friend, *Applied Physics Letters*, 2003, **82**, 1123.
13. S. Alkis, T. Özta, L. E. Aygün, F. Bozkurt, A. K. Okyay and B. Ortaç, *Opt. Express*, 2012, **20**, 21815-21820.
14. R. J. Smith, P. J. King, M. Lotya, C. Wirtz, U. Khan, S. De, A. O'Neill, G. S. Duesberg, J. C. Grunlan, G. Moriarty, J. Chen, J. Wang, A. I. Minett, V. Nicolosi and J. N. Coleman, *Advanced materials*, 2011, **23**, 3944-3948.
15. J. N. Coleman, M. Lotya, A. O'Neill, S. D. Bergin, P. J. King, U. Khan, K. Young, A. Gaucher, S. De, R. J. Smith, I. V. Shvets, S. K. Arora, G. Stanton, H. Y. Kim, K. Lee, G. T. Kim, G. S. Duesberg, T. Hallam, J. J. Boland, J. J. Wang, J. F. Donegan, J. C. Grunlan, G. Moriarty, A. Shmeliov, R. J. Nicholls, J. M. Perkins, E. M. Grieveson, K. Theuwissen, D. W. McComb, P. D. Nellist and V. Nicolosi, *Science*, 2011, **331**, 568-571.
16. A. Meerschaut and C. Deudon, *Materials Research Bulletin*, 2001, **36**, 1721-1727.
17. S. Lebegue and O. Eriksson, *Physical Review B*, 2009, **79**.

18. G. Cunningham, M. Lotya, C. S. Cucinotta, S. Sanvito, S. D. Bergin, R. Menzel, M. S. P. Shaffer and J. N. Coleman, *ACS Nano*, 2012, **6**, 3468-3480.
19. K. Zhou, S. Jiang, C. Bao, L. Song, B. Wang, G. Tang, Y. Hu and Z. Gui, *RSC Advances*, 2012, **2**, 11695-11703.
20. Z. Zeng, T. Sun, J. Zhu, X. Huang, Z. Yin, G. Lu, Z. Fan, Q. Yan, H. H. Hng and H. Zhang, *Angew Chem Int Ed Engl*, 2012, **51**, 9052-9056.
21. Y. Du, Z. Yin, J. Zhu, X. Huang, X. J. Wu, Z. Zeng, Q. Yan and H. Zhang, *Nature communications*, 2012, **3**, 1177.
22. Y.-H. Lee, X.-Q. Zhang, W. Zhang, M.-T. Chang, C.-T. Lin, K.-D. Chang, Y.-C. Yu, J. T.-W. Wang, C.-S. Chang, L.-J. Li and T.-W. Lin, *Advanced Materials*, 2012, **24**, 2320-2325.
23. Z. Liu, S. Peng, Q. Xie, Z. Hu, Y. Yang, S. Zhang and Y. Qian, *Advanced materials*, 2003, **15**, 936-940.
24. Z. He, S. H. Yu, X. Zhou, X. Li and J. Qu, *Advanced Functional Materials*, 2006, **16**, 1105-1111.
25. C.-C. Lin, W.-F. Lee, M.-Y. Lu, S.-Y. Chen, M.-H. Hung, T.-C. Chan, H.-W. Tsai, Y.-L. Chueh and L.-J. Chen, *Journal of Materials Chemistry*, 2012, **22**, 7098-7103.
26. R. J. Mehta, C. Karthik, W. Jiang, B. Singh, Y. Shi, R. W. Siegel, T. Borca-Tasciuc and G. Ramanath, *Nano Letters*, 2010, **10**, 4417-4422.
27. W. Zhao, M. Fang, F. Wu, H. Wu, L. Wang and G. Chen, *Journal of Materials Chemistry*, 2010, **20**, 5817.
28. B. O'Regan and M. Gratzel, *Nature*, 1991, **353**, 737-740.
29. S. Thomas, T. G. Deepak, G. S. Anjusree, T. A. Arun, Shantikumar V. Nair and A. Sreekumaran Nair, *Journal of Materials Chemistry A*, 2014, **2**, 4474-4490.
30. S. Ahmad, E. Guillen, L. Kavan, M. Gratzel and M. K. Nazeeruddin, *Energy & Environmental Science*, 2013, **6**, 3439-3466.
31. X. Yang, S. Zhang, K. Zhang, J. Liu, C. Qin, H. Chen, A. Islam and L. Han, *Energy & Environmental Science*, 2013, **6**, 3637-3645.
32. J.-M. Li, *Applied Physics A*, 2009, **99**, 229-235.
33. J.-M. Li, *Nano Letters*, 2008, **8**, 1382-1385.
34. M. Bodaghi, A. R. Mirhabibi, H. Zolfonun, M. Tahriri and M. Karimi, *Phase Transitions*, 2008, **81**, 571-580.
35. R. Gers, E. Climent, D. Legendre, D. Anne-Archard and C. Frances, *Chemical Engineering Science*, 2010, **65**, 2052-2064.
36. V. Sepelak, S. Begin-Colin and G. Le Caer, *Dalton transactions*, 2012, **41**, 11927-11948.
37. N. D. Boscher, C. J. Carmalt and I. P. Parkin, *European Journal of Inorganic Chemistry*, 2006, **2006**, 1255-1259.
38. S. Bose, P. Raychaudhuri, R. Banerjee, P. Vasa, & P. Ayyub, *Phys Rev Lett*, 2005, **95**, 147003 .
39. Y. Wu, M. An, R. Xiong, J. Shi and Q. M. Zhang, *Journal of Physics D: Applied Physics*, 2008, **41**, 175408.
40. N. Staley, J. Wu, P. Eklund, Y. Liu, L. Li and Z. Xu, *Physical Review B*, 2009, **80**.
41. S. Chiang, G. K. Wertheim and F. J. DiSalvo, *Solid State Communications*, 1976, **19**, 75-78.
42. K. H. Bennemann and J. B. Ketterson, *The Physics of Superconductors: Vol. II: Superconductivity in Nanostructures, High-Tc and Novel Superconductors, Organic Superconductors*, Springer, 2004.
43. S. Bose, P. Raychaudhuri, R. Banerjee, P. Vasa and P. Ayyub, *Physical Review Letters*, 2005, **95**, 147003.
44. F. Malara, M. Manca, M. Lanza, C. Hubner, E. Piperopoulos and G. Gigli, *Energy & Environmental Science*, 2012, **5**, 8377-8383.
45. L. Yi, Y. Liu, N. Yang, Z. Tang, H. Zhao, G. Ma, Z. Su and D. Wang, *Energy & Environmental Science*, 2013, **6**, 835-840.